An Efficient Inductive Power Transfer Topology for Electric Vehicle Battery Charging

Jitendra Kumar Nama, *Student Member, IEEE*, Arun Kumar Verma, *Senior Member, IEEE*, Manaswi Srivastava, *Student Member, IEEE*, and Pavan Singh Tomar, *Student Member, IEEE*

***Abstract*—Recently available high-frequency power converter topologies for inductive power transfer (IPT) system utilize either zero voltage switching (ZVS) or zero current switching (ZCS) based power electronic converters while maintaining a near sinusoidal current for limited power transfer range. However, achieving ZVS or ZCS for all power switches simultaneously is still a challenging task in IPT systems. In this article, an improved zero-voltage zero-current switching (ZVZCS) IPT topology and its switching pattern are proposed. ZVS is achieved by optimizing the classical series compensation and additionally, an auxiliary network is employed to achieve ZCS. The proposed concept is verified by using MATLAB/Simulink based simulations for resistive and battery load. Finally, the practical viability of the proposed topology is validated by the results obtained using a laboratory prototype rated for 1.1 kW, 85 kHz. An efficiency of 91.26% is achieved with ZVZCS for a full dynamic power transfer range of 20 W–1.1 kW.**

***Index Terms*—Battery chargers, dc–dc power converters, electric vehicles (EVs), inductive charging, soft switching, wireless power transmission.**

NOMENCLATURE

V_{DC}	Input dc source voltage.
I_{DC}	Input dc source current.
C_{a1}, C_{a2}, C_a	Capacitance of input dc-link capacitor.
$I_{C_{a1}}, I_{C_{a2}}$	Current through capacitors C_{a1}, C_{a2}, respectively.
$S_1 - S_4$	H-bridge inverter active switches.
$P_{S_1} - P_{S_4}$	Gating signals for switches $S_1 - S_4$, respectively.
$I_{S_1} - I_{S_4}$	Current passing through switches S_1, S_2, S_3, S_4, respectively.
$V_{S_1} - V_{S_4}$	Voltage across switches $S_1 - S_4$, respectively.
$D_1 - D_4$	Antiparallel body diodes of active switches $S_1 - S_4$, respectively.
$D_5 - D_8$	Output rectifier diodes.
$C_{S1} - C_{S4}$	Parallel parasitic capacitors $C_{S1} - C_{S4}$, respectively.
$I_{C_1} - I_{C_4}$	Current through $C_{S1} - C_{S4}$.
T_A	Ancillary transformer.
T_{A1}, T_{A2}	Primary and secondary turns of ancillary transformer.
$I_{T_{A1}}, I_{T_{A2}}$	Current passing through primary, secondary coil ancillary transformer T_{A1}, T_{A2} coils, respectively.
L_A	Ancillary inductor.
I_{L_A}	Current through L_A.
L_1, L_2	Transmitter and receiver coil inductor.
I_{L_1}, I_{L_2}	L_1 and L_2 current.
C_1, C_2	Compensation capacitor for inductors L_1 and L_2.
V_{C_1}, V_{C_2}	Voltage across capacitors C_1 and C_2.
M	Mutual inductance between L_1 and L_2 coils.
k_c	Coefficient of mutual coupling between inductors L_1 and L_2.
C_F	Filter capacitor.
I_{C_F}	Current through filter capacitor C_F.
B	Battery as load.
V_B	Voltage across B.
I_B	Battery B charging current.
R_B	Equivalent battery resistance.
V_{ds}	MOSFET drain to source voltage.
I_D	MOSFET drain current.
V_D	Diode forward biased voltage.
U_{AB}	Root mean square value of voltage across points *A*, *B*.
u_{AB}	Instantaneous value of voltage across points *A*, *B*.
U_{ab}	Root mean square value of voltage across points *a*, *b*.
u_{ab}	Instantaneous value of voltage across points *a*, *b*.
ω_0	Resonance frequency in radian per seconds.
T_D	Time period when all switches are OFF.
T_{ON}	Time period when two opposite leg switches are ON.
K	Turn ratio of wireless transformer.
P_{cu}	Copper losses.
P_{core}	Core losses.

Manuscript received January 28, 2020; revised April 19, 2020 and July 2, 2020; accepted August 9, 2020. Date of publication August 21, 2020; date of current version November 19, 2020. This work was supported by SERB-DST India under Grant ECR/2016/001920. Paper 2019-TSC-1436.R2, presented at the 2018 8th IEEE India International Conference on Power Electronics, Jaipur, India, Dec. 13–15, and approved for publication in the IEEE TRANSACTIONS ON INDUSTRY APPLICATIONS by the Transportation Systems Committee of the IEEE Industry Applications Society. *(Corresponding author: Jitendra Kumar Nama.)*

The authors are with the Department of Electrical Engineering, Malaviya National Institute of Technology, Jaipur 302017, India (e-mail: jknama1000@gmail.com; arun.ee@mnit.ac.in; 2016ree9506@mnit.ac.in; 2017REE9503@MNIT.AC.IN).

Color versions of one or more of the figures in this article are available online at https://ieeexplore.ieee.org.

Digital Object Identifier 10.1109/TIA.2020.3018419

I. Introduction

THE increasingly global economy is facing the demolition of fuel resources along with hazardous disturbances in environmental conditions. Moreover, it has spurred the emergence of sustainable technologies leading to innovations in major carbon contributors, i.e., transportation [1], [2]. Therefore, electric vehicles (EVs) are adopted as a solution to diminish the environmental effects caused by carbon-based fuels [2], [3]. Furthermore, the EVs market opens a new opportunity for human beings to expand the life expectancy of transportation at a lower cost [1], [3]. In the past, the battery technology (BT) and power shaping technologies are the limitations to put EVs out of market success. However, BT has been evolved with high energy density, lesser weight, and high efficiency in a few past decades [4]. Additionally, efficient energy storage device improves overall performance while used with a suitable power shaping circuit. A dc–dc power conditioning configuration having subservient power losses, durability, reliable energy transfer, and increased charging-discharging cycles are exercised by researchers and industries [1]–[4].

Nowadays, efficient, fast chargers are deployed for short driving range with human safety concerns. In the present scenario, the inductive power transfer (IPT)-based typologies are adopted as safer battery charging (BC) solutions during EV stationary and dynamic mode. Compensation networks are presented to crimp the circuit impedance for improving the overall efficiency of the converter. However, the number of active and passive elements of the circuits comprises with the complexity of the configuration [5]. The right solution further improves the driving range, maintenance cycle, reduced carbon footprint, and end-user economy. Therefore, converter selection plays a vital role in EV's flow in the market. Consequently, it supports decrement in environmental problems produced by transportation issues expertly [6].

The classical series-series capacitor compensation based IPT topology is one of the most preferred network arrangement adopted by industries because of its structure simplicity and operational stability for varying coils distance [7]. This network presents a low-cost solution but compromises its efficiency, power transfer capability, high resonant peaks, and control accuracy for variant loading. In [7], an algorithm for phase control is presented to enhance efficiency bandwidth; however, the expense results as a sophisticated control strategy for variant frequency. In [8], issues generated by variable frequency are mitigated by defining the control boundary in the optimal frequency range. The control solutions presented in [7] and [8] only supports clam to provide higher efficiency by maintaining zero voltage switching (ZVS) for IPT system. The topological advancement in [9] has been done by a new coil support network using intermediate *L–C* series compensated structure at both the transmitter and receiver end. This configuration increases weight at the vehicle side, which is mitigated in [10], by placing both coils on the primary side. The solution presented in [9] and [10] provides magnetic flux support in misalignment condition but decreases the beauty of simplicity in calculation and control operation. A solution to the issues present in [9] and [10] as an isolated tank network to support IPT is addressed in [11] by incorporating an H-bridge high-frequency transformer with *L–C* tank network. However, it increases the size, weight, and volume of the whole system while reducing peak efficiency.

Therefore, a solution as the reconstruction of the passive component's network is presented in [12]–[17] to mitigate issues sprouted by an additional magnetically isolated resonant tank. In [12] and [13], a symmetrical filter network is cascaded with loosely coupled transformer coils to improve the performance of the system for a long duration. However, these topologies implement magnetically isolated inductors, which increase weight, volume, complexity in tuning method, and decrease efficiency. These issues are addressed in [14] and [15] by employing asymmetrical compensation using the *LCC-C* network configuration. The analysis of claims presented in [12]–[15] are comparatively studied in [16] and [17], and it is found that for the same coil design, *LCC–LCC* network is suitable for stationary IPT and *LCC-C* for dynamic IPT. However, it suffers distortions in the case of vehicle side topology and clearance variations. Therefore, Zhang *et al.* [16] and Li *et al.* [17] direct to find a different solution utilizing series *C–C* compensation. In [18]–[20], a solution to stabilize soft switching for a wide operating range, improved efficiency, performance for the strongly coupled transformer-based dc–dc converter is presented. In [21] and [22], the auxiliary network is adopted to enhance the performance of resonant IPT topology based on [18]–[20]. The constant losses have been increased because of additional magnetics while stable operation with improved efficiency is obtained. Likewise, a solution for resonant IPT based series *C–C* compensated topology is presented in [23]. In this view point, IPT with auxiliary circuit can mitigate issues present in voltage source inverter (VSI) fed converter based network.

In this article, the proposed topology utilizes classical series *L–C* compensation with a small size auxiliary components to make ZVS along with zero current switching (ZCS). The proposed topology offers a constant output voltage even if the input is subjected to a wide range of voltage variations. The output current can easily be controlled from the input side voltage, which eliminates the requirement of a high-power processor for controlling operation, and the cost for the converter is effectively reduced. A laboratory prototype has been developed and tested for resistive and battery load for full BC range. Fig. 1 shows the general overview of the proposed topology in which two stages of the converter have been controlled by using modified pulsewidth modulation (MPWM) separately. The pulses are generated at 85 kHz switching frequency in MPWM mode to achieve zero-voltage zero-current switching (ZVZCS) to deliver power up to 1.1 kW, and performance results are presented.

The rest of the article is organized into the following sections. The operating principle of the proposed converter is discussed in Section II. The study of circuit parameter design is presented in Section III. Section IV discussed various steps of the hardware development process for laboratory prototype. Simulation

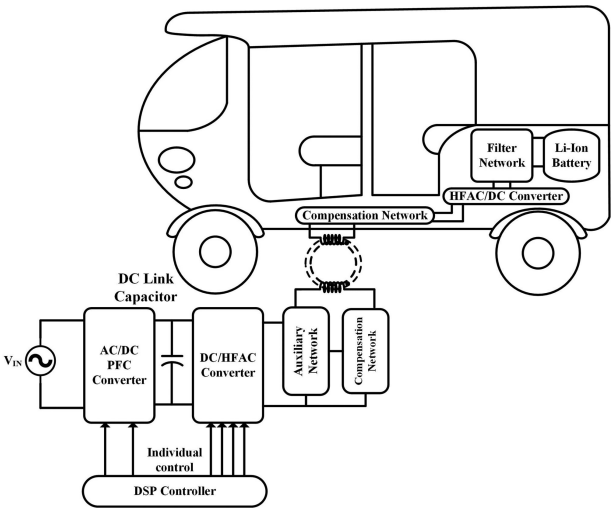

Fig. 1. General configuration of wireless battery charger topology.

and hardware results are discussed in Section V. Finally, the conclusion has been drawn in Section VI.

II. Operating Principle of the Proposed Converter

Active switches $S_1 - S_4$ at primary side and diodes $D_5 - D_8$ at secondary side forms a H-bridge (conventional). Moreover, C_{a1} and C_{a2} act as potential divider at the input with ancillary L_A and T_A to maintain the soft-switching feature of the circuit with BC. The primary and secondary side of the circuit is coupled with L_1 and L_2 with C_1 and C_2, respectively. The operation of the converter is controlled by using MPWM in [22].

The following assumptions are considered to understand the operating principle of the proposed converter.

1) All active and passive devices consisting of transformer, dc source, switches, diodes, and capacitors are ideal including internal switch diode and capacitance.
2) Electrical series resistance of inductor and interwinding capacitance of transformer are neglected.
3) Voltage divider capacitors ($C_a = C_{a1} = C_{a2}$) and C_F are large enough to maintain constant voltage at input and output terminals of the converter.
4) The effects of the magnetizing inductance of T_A are neglected.

A. Operation of Proposed Converter

The operating principle of the proposed topology in steady state is divided into eight modes (modes I–VIII) as shown in Fig. 2 and the operating waveforms are shown in Fig. 3.

1) Mode I ($t_0 \le t < t_1$), Fig. 2(a): Before time instant t_0, lagging current $(I_{L_1} + I_{L_A})$ is flowing from D_1 and S_2, Therefore, at t_0 instant, the switch S_1 is turned ON with ZVS. Furthermore, a potential difference between AC and CB is created and current I_{L_A} start rising from $I_{L_A(t_0)}$

$$i_{L_A} = \begin{cases} \dfrac{|V_{C_{a1}} - V_{C_{a2}}|}{2L_A} T_{\text{ON}} - i_{L_A(t_0)} & \text{If} \rightarrow R_{ON(S_1-S_4)} \neq 0 \\ |V_{C_{a1}} - V_{C_{a2}}| = 0 \;||\; i_{L_A} = 0 & \text{If} \rightarrow R_{ON(S_1-S_4)} = 0 \end{cases}. \quad (1)$$

2) Mode II ($t_1 \le t < t_2$), Fig. 2(b) and (c): Before t_0, switch S_1 is conducting and switch current difference $(i_{S_1} - i_{S_2})$ is flowing from T_A $(I_{T_{A1}} + I_{T_{A2}} = I_{L_A})$.

Applying KCL at points *A* and *B* and using low energy conservation

$$i_{C_{S1}} + i_{C_{S4}} = i_{T_{A2}} + i_{L_1} \quad (2)$$

$$2i_{C_{S1}} = i_{L_1} + \frac{i_{L_A}}{2}. \quad (3)$$

At the starting of this mode, S_1 is turned OFF when S_3, S_4 are already OFF, and S_2 is still conducting. The dominant inductance L_1 is now in cutoff from dc power source, and $I_{L_1} + \frac{I_{L_A}}{2}$ starts charging switch peracetic capacitor C_{S1}. At instant t_{11}, $V_{C_{S1}}$ reaches V_{DC}. After t_{11}, I_{L_1} finds a path by forcing the change in I_{L_A}. The inductor L_A rejects this change and a current starts from S_2 to S_4, which discharges C_{S4}. After C_{S4} voltage reaches zero, D_4 turns ON and this freewheeling results in the decrement of I_{S_2} to zero or ZCS for switch S_2

$$t_{(V_{C_{S1}}=V_{DC})} = \frac{\frac{1}{2}C_{S3}V_{DC} - \left(i_{L_1(t_{1-})} + \frac{i_{L_A(t_{1-})}}{2}\right)}{i_{L_1(t)} + \frac{i_{L_A(t)}}{2}}. \quad (4)$$

3) Mode III ($t_2 \le t < t_3$), Fig. 2(d) and (e): This mode starts from S_2 ZCS turn OFF while other switches are already OFF. During this mode, the peracetic capacitor C_{S2} starts charging till t_{21} up to V_{DC} and the current I_{L_A} decrementing toward zero after attaining its positive peak. After t_{21}, the current $I_{L_1} + \frac{I_{L_A}}{2}$ finds its path by discharging capacitors C_{S3}, C_{S4} and turns ON the diodes D_2, D_4

$$t_1 > 2C_{S1}\frac{V_{DC}}{i_{L_1(t_0)} + \frac{i_{L_A(t_0)}}{2}}. \quad (5)$$

The voltage stress across switch is given by the following expression:

$$v_{S1} = V_{DC} + v_{C_1} \quad (6)$$

$$v_{S4} = -v_{C_1}. \quad (7)$$

4) Mode IV ($t_3 \le t < t_4$), Fig. 2(f): In this mode of operation, S_4 is turned ON with ZVS as D_4 is on and the voltage across S_4 is near zero. The auxiliary inductor current I_{L_A} is increasing linearly in a positive direction after attaining its negative peak.

5) Mode V ($t_4 \le t < t_5$), Fig. 2(g): In this mode, S_3 is turned ON with ZVS. I_{AB} starts following the sinusoidal wave shape, and voltage across S_3, S_4 are zero as its path got completed.

6) Mode VI ($t_5 \le t < t_6$), Fig. 2(h) and (i): This mode starts by turning OFF S_3, which triggers C_{S3} charging up to V_{DC} at t_{51}. The auxiliary inductor current I_{L_A} is decreasing after attaining its peak and I_{L_1}, I_{L_A} forces I_{S_4} to reduce for ZCS turn-OFF condition.

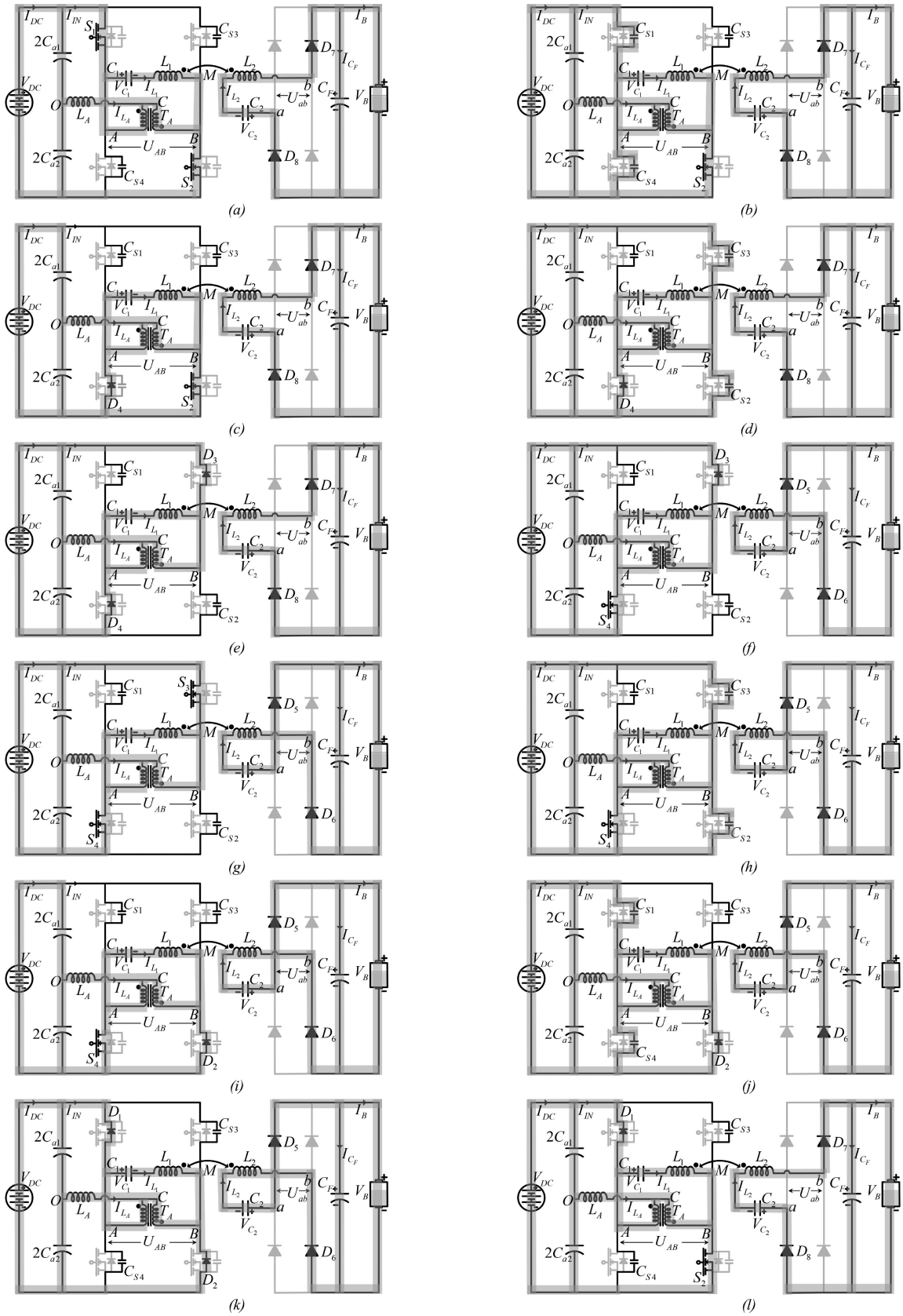

Fig. 2. Operating modes of proposed battery charger topology. (a) Mode I ($t_0 \leq t < t_1$). (b) Mode II (part-1) ($t_1 \leq t < t_{11}$). (c) Mode II (part-2) ($t_{11} \leq t < t_2$). (d) Mode III (part-1) ($t_2 \leq t < t_{21}$). (e) Mode III (part-2) ($t_{21} \leq t < t_3$). (f) Mode IV ($t_3 \leq t < t_4$). (g) Mode V ($t_4 \leq t < t_5$). (h) Mode VI (part-1) ($t_5 \leq t < t_{51}$). (i) Mode VI (part-2) ($t_{51} \leq t < t_6$). (j) Mode VII (part-1) ($t_6 \leq t < t_{61}$). (k) Mode VII (part-2) ($t_{61} \leq t < t_7$). (l) Mode VIII ($t_7 \leq t < t_8$).

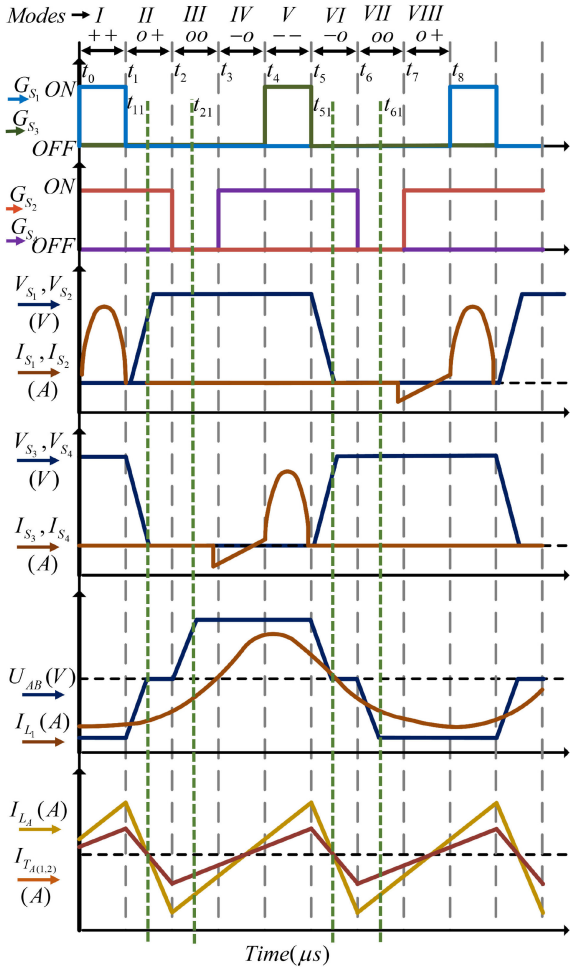

Fig. 3. Theoretical operating waveform of proposed wireless converter topology.

7) Mode VII ($t_6 \leq t < t_7$), Fig. 2(j) and (k): In this mode, S_4 turned OFF at ZCS and $V_{C_{S4}}$ rises up to V_{DC} at t_{61}. After t_{61}, I_{L_A} starts incriminating in positive direction. The diodes D_1 and D_2 turned ON and power is feedback to the source.

8) Mode VIII ($t_7 \leq t < t_8$), Fig. 2(l): During this mode of operation, switch S_2 is turned ON with ZVS and current shifts from D_2 to S_2.

During mode, I to VIII constant voltage and current are maintained in the battery.

B. Working of Ancillary Network

The ancillary and transmitter coil resonant network is shown in Fig. 5. The voltage across L_A is obtained from applying KVL as follows:

$$V_{C_{a1}} = V_{C_{a2}} = \frac{V_{DC}}{2} \tag{8}$$

$$\left.\begin{aligned} v_{OC} = v_{L_A} &= \frac{V_{DC}}{2} - v_{CD} - v_B \\ &= \frac{V_{DC}}{2} - \left(v_A - \frac{V_{DC}}{2}\right) - v_B \\ &= V_{DC} - v_A - v_B \end{aligned}\right\}. \tag{9}$$

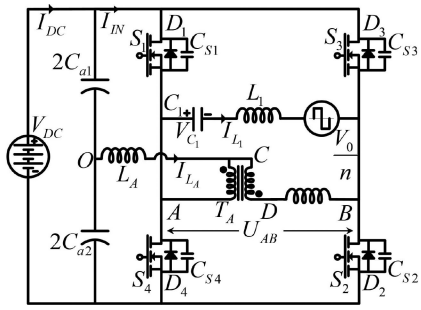

Fig. 4. Simplified network with battery load refereed at transmitter coil side.

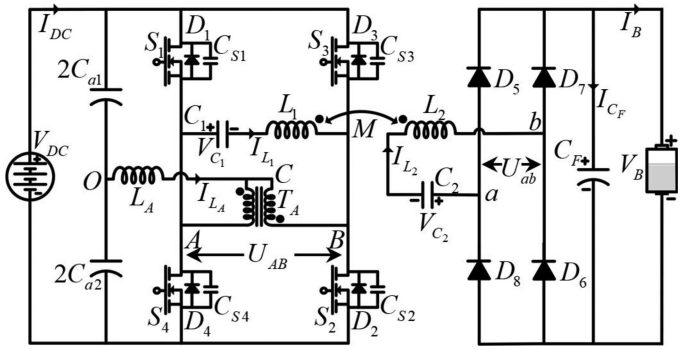

Fig. 5. Proposed network configuration of EV battery charger.

Expression (9) shows the waveform of $v_{OC} = V_{L_A}$, which is complimentary of v_{AB}. This shows the current in L_A is high for light loading condition and complimentary for heavy loading condition.

When the voltage $v_{AB} = V_{DC}$ or $-V_{DC}$ and $v_{C_{a1}} = v_{C_{a2}} = \frac{V_{DC}}{2}$ than from expression (9) $V_{L_A} = 0$. Therefore, current in inductor L_A remains unchanged. The value of i_{L_A} is expressed by (10) when $v_{C_{a1}} \neq v_{C_{a2}}$ and either $S_1 - S_2$ or $S_3 - S_4$ in ON state.

The current expression for i_{L_a} can be derived from Fig. 4 as follows:

$$\left.\begin{aligned} i_{L_A} &= i_{T_{A1}} + i_{T_{A2}} \\ i_{T_{A1}} &= i_{T_{A2}} \\ i_{T_{A1}} &= i_{T_{A2}} = \frac{1}{2} i_{L_A} \end{aligned}\right\}. \tag{10}$$

By applying KVL in Fig. 5 and (10), the magnitude of i_{L_A} can be given from the following expression:

$$\left.\begin{aligned} I_{L_A} = \\ \tfrac{1}{4}\tfrac{V_{DC}}{L_A}(T - T_{ON}) + \tfrac{1}{2}\tfrac{|V_{C_{a1}} - V_{C_{a2}}|}{L_A}(T_D)\,\tfrac{T}{2} \end{aligned}\right\} \tag{11}$$

$$I_{L_A \max} = 2 I_{L_A}(1 - T_D) \tag{12}$$

$$T_D = \frac{T}{2} - T_{ON} \tag{13}$$

$$T_{ON} = t_1 - t_0 = t_6 - t_5. \tag{14}$$

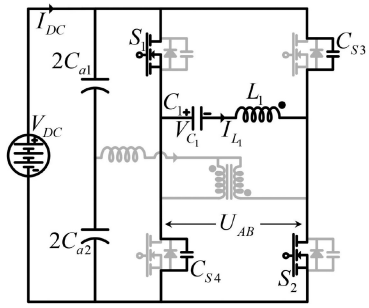

Fig. 6. Network operation in positive half-cycle.

III. Parameter Design

A. Compensation Capacitance

The series compensation capacitance is calculated by using the following relation:

$$C = \frac{1}{\omega_0^2 L} \tag{15}$$

where C is compensation capacitance, and L is the compensated inductance.

B. Switch Rating

1) Transient Analysis: The calculation of the current at the starting of the converter has been done in the switch's active state (positive half-cycle of transmission coil current). Fig. 6 presents the simplified primary network for calculation of ω_0 and switch's ON-time T_{ON}.

By using KVL in a simplified primary network shown in Fig. 5, we have

$$L_1 \frac{di_{L_1}(t)}{dt} + R_1 i_{L_1}(t) + \frac{1}{C_1}\int_0^t i_{L_1}(t)\cdot dt = u_{AB}(t). \tag{16}$$

By solving and simplifying (16), the output current waveform is given as

$$i_{L_1}(t) = e^{at}[C_1\cos(at) + C_2\cos(bt)] \tag{17}$$

where $a = (-\frac{R_1}{2L_1})$, $b = \sqrt{(a)^2 - \frac{1}{L_1 C_1}}$, and C_1 and C_2 are constants that can be derived from network initial conditions.

The other solution of (9) is given by solving in the frequency domain using the Laplace transform where

$$K_1 = 1 - \frac{2e^a\sqrt{L_1}}{\sqrt{4L_1 - R_1^2 C_1}}, K_2 = \frac{\sqrt{4L_1 - R_1 L_1 C_1}}{2L_1\sqrt{C_1}},$$

$$K = \frac{1}{R}\frac{\sqrt{4L_1 - R_1^2 C_1}}{\sqrt{C_1}}$$

$$i_{L_1}(t) = K_1\sin(K_2(t) + \tan^{-1}(K_3)). \tag{18}$$

Eq. (4) is used for determining the current peak and first zero crossing (T_Z) in the circuit. In the proposed topology, successful ZCS is achieved by taking T_{ON} less than T_Z.

2) Steady-State Analysis: Applying the Fourier analysis in Fig. 5, we have

$$U_{AB(n)} = \frac{4V_{DC}}{n\pi}\cos(n\alpha) \tag{19}$$

$$I_{AB(n)} = \frac{1}{Z_n}U_{AB} \tag{20}$$

$$Z_n = \sqrt{K^4 R_B^2 + \left(n\omega\left(L_1 + K^2 L_2\right) - \left(\frac{C_1 C_2}{n\omega(K^2 C_1 + C_2)}\right)\right)^2} \tag{21}$$

$$\psi_n = \tan^{-1}\frac{n\omega\left(L_1 + K^2 L_2\right) - \frac{C_1 C_2}{n\omega(K^2 C_1 + C_2)}}{K^2 R_B} \tag{22}$$

$$R_B = \frac{V_B}{I_B}. \tag{23}$$

The proposed transmitter coil network has a high-quality factor and a high resonant frequency. Therefore, the fundamental component has a very high magnitude and produces the dominating current. The expression for the fundamental component can be derived from (19) and (20). The maximum current passing through L_1 and switches ($S_1 - S_4$) is given as follows:

$$I_{AB(01)} = \frac{4V_{DC}}{Z_{01}\pi}\cos(\alpha) \tag{24}$$

$$I_{AB(01)\max} = \sqrt{2} I_{AB(01)} \tag{25}$$

$$I_{S1-S4(\max)} = I_{AB(01)\max} + I_{L_A\max}. \tag{26}$$

The voltage rating of C_1 is calculated by using current second balance and expression as follows:

$$V_{C_1} = \frac{4V_{DC}}{C_1 Z_{01}}\cos(\alpha) \tag{27}$$

where $\alpha = \pi(1 - 2\frac{T_{ON}}{T})$.

Alternatively, the rating of the switch can also be calculated by using the following relation:

$$V_{ds} > Vs + K(V_B + V_D) \tag{28}$$

$$V_{ds} > 140 + 1(135 + 1.4) \tag{29}$$

$$V_{ds} > 276.4\,\text{V}. \tag{30}$$

The typical MOSFETs can withstand three times their average current rating in a nonrepetitive situation. So, a good conservative current rating is calculated by using the following relation:

$$I_D > 3X I_{s,\text{avg}} \tag{31}$$

$$I_D > 3X6 \tag{32}$$

$$I_D > 18\,\text{A}. \tag{33}$$

Therefore, the rating of the power switch selected must have voltage and current rating greater than 276.4 V and 18 A. Hence, the IRFP460 is selected for this converter because it is having 500 V and 20 A rating.

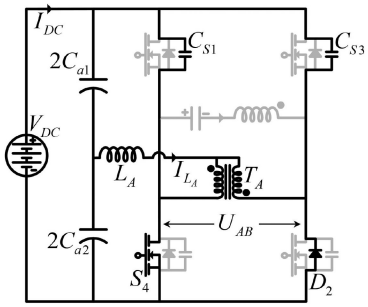

Fig. 7. Simplified circuit to determine auxiliary component parameter.

C. Auxiliary Components

The value of auxiliary capacitors is decided in such a way that they maintain constant voltage at the input of the converter. Meanwhile, the auxiliary inductor acts as a constant current source during peak and dead time conditions. The auxiliary inductor with a transformer is used to supply the necessary current required to achieve ZCS. The auxiliary transformer holds a sudden change in U_{AB} and provides a return path to inductor L_1 current. The transformer has a 1:1 voltage ratio with minimum possible leakage inductance and series resistance. Fig. 7 shows the simplified circuit for the calculation of auxiliary components [21], [22].

Applying KVL in Fig. 6 network, we have

$$\frac{\Delta i_{C_a}}{C_a}\Delta t - L_a\frac{\Delta I_{C_a}}{\Delta t} - M\frac{\Delta I_{C_a}}{\Delta t} = 0 \tag{34}$$

$$M\frac{\Delta i_{C_a}}{\Delta t} + M\frac{\Delta I_{C_s} - \Delta i_{C_a}}{\Delta t} - \frac{\Delta I_C}{C_S}\Delta t = 0. \tag{35}$$

By using (34) and (35), Δt and $C_a = C_{a1} = C_{a2}$ are calculated, Δt is the time when the diode of a switch is ON makes it go ZVS turn ON. The total turn-ON time included for a switch in half-cycle is $T_{\text{on}} + \Delta t$.

These designed parameters provide ZVS for all four switches and ZCS for two switched in half-cycle. The parameters used in the simulation are described in Table I.

1) Loss Calculation in Auxiliary Network: Cu loss of the auxiliary network is given by the following equation:

$$P_{\text{cu}} = I^2R \tag{36}$$

where *I* belongs to auxiliary inductor and transformer current (I_{L_A} and $I_{T_{A(1,2)}}$).

The cu losses are calculated for worst case where I_{L_A}=2 A, R_{L_A}=170 mΩ, $I_{T_{A(1,2)}}$=2 A, and $R_{T_{A(1,2)}}$=330 mΩ [24].

Therefore, Cu loss in the auxiliary inductor is calculated as 680 mW and Cu loss in transformer is 1.32 W.

The core losses per unit volume for transformer and inductor are calculated by using the following equation (when the converter is operating at constant frequency):

$$P_{\text{core}} = aB_{pk}{}^bV. \tag{37}$$

The value of a is 0.043, b is 1.5, and B_{pk} is calculated as approximately 1 T for Sendust Core.

TABLE I
SIMULATION AND EXPERIMENTAL SETUP DESIGN PARAMETERS

Parameters	Symbol	Details
Switching frequency	f	85 kHz
DC link Capacitor	C_{a1}, C_{a2}	47μF
Auxiliary series inductor	L_A	17.7 μH
Auxiliary transformer ratio	N	1 : 1
Nominal power		550 VA
Nominal voltage		325 V
Nominal leakage inductance		0.4 μH
Magnetizing resistance		20 $k\Omega$
Magnetizing inductance		8 mH
Primary coil inductance	L_1	232 μH
Secondary coil inductance	L_2	232 μH
Coefficient of coupling	k_C	0.16
Mutual inductance	M	37.2 μH
Compensation capacitor primary coil	C_1	15.8 nF
Compensation capacitor secondary coil	C_2	15.6 nF
Electrical series resistance of primary coil and compensation capacitor	R_1	0.2 Ω
Electrical series resistance of secondary coil and compensation capacitor	R_2	0.2 Ω
Switch peracetic capacitance	C_{S1}, C_{S2}, C_{S3}, C_{S4}	870 pF
Switch on resistance		270 $m\Omega$
Rectifier diode on state voltage drop		0.45 V
Diode on state resistance		80 $m\Omega$
Filter Capacitance	C_F	47 μF
Battery type		Li-Ion
Battery voltage	V_B	120 V
Load resistance		19 Ω
Switch S_1, S_3 pulse duty cycle		45.5 %
Switch S_2, S_4 pulse duty cycle		48.5 %

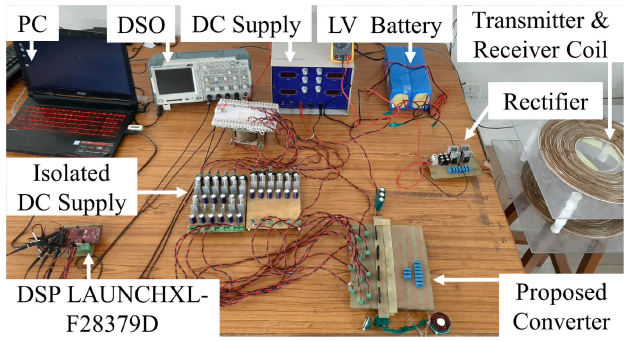

Fig. 8. Developed laboratory prototype for BC at moderate power transfer.

The core volume for the inductor is 430 mm^3 (0_41450TC, wire − 6/38, AWG22) and transformer core volume is 1164 mm^2 (0_41610TC, wire − 3/38, AWG22). Hence, the calculated power loss for L_A and T_A is 18.49 and 50.05 mW, respectively, by using (37) [25], [26].

IV. LABORATORY PROTOTYPE

To validate the circuit analysis and simulation results, a laboratory prototype of 1.1 kW at 85 kHz is developed and tested for BC characteristics as shown in Figs. 8 and 9 and its specifications are listed in Table II.

The developed prototype primarily composed of five major parts: dc power supply, proposed dc–dc converter, IPT transmitter and receiver coil set, bridge rectifier, resistive, and battery load. A low voltage isolated dc power supply based on bridge

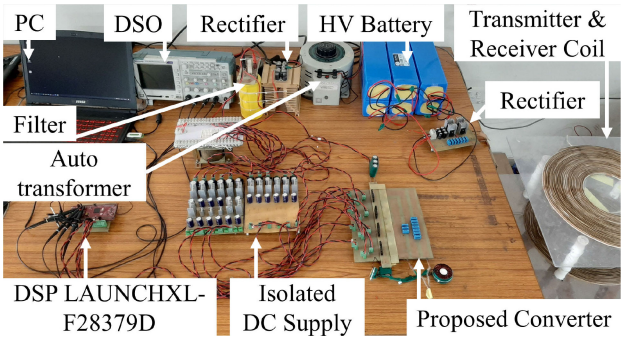

Fig. 9. Developed laboratory prototype for BC at high power transfer.

TABLE II
SPECIFICATION OF HARDWARE COMPONENTS

Specifications	Part No.
Power MOSFET	IRFP460
Ultra fast rectifier diode	MUR3060
Gate Driver IC	TC4420, TC4429
Opto-isolator IC	6N137
Line driver IC	74LS04, 74LS07
Digital isolator	ISO7762
Load Resistance	0-25 Ω, 10A wire wound
Voltage regulator IC	LM7815, LM7805
Switch charge control diode	UF4007
DSP Controller	LUNCHXL F28379D
Lithium-Ion	120V, 1.14kVA

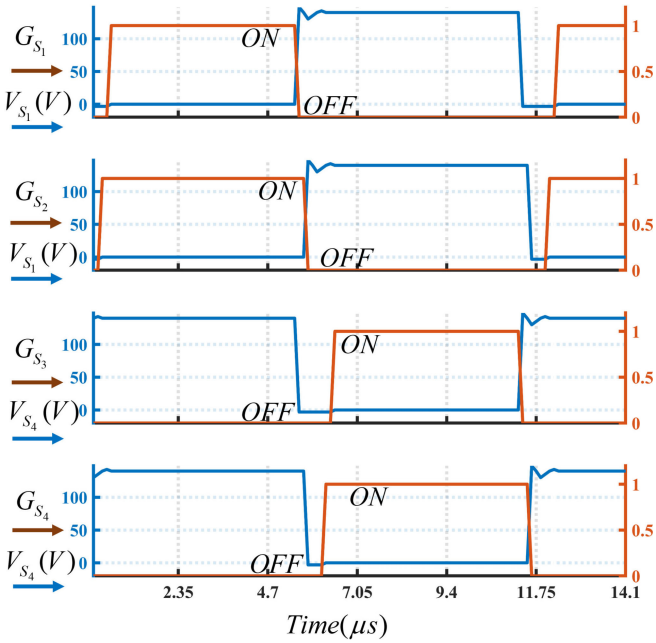

Fig. 10. ZVS turn-ON for $S_1 - S_4$.

rectifier, and linear voltage regulator is developed to active pulse triggering circuit to the dc–dc converter. Open-loop control is used for testing at different charging states of the battery.

In the proposed converter, a split electrolytic capacitor is used to maintain a constant voltage at the input terminal of H-bridge. The driver circuit is placed very near to the switch by utilizing surface mount device technology to reduce any line inductance and circuit positioning effects. The transmitter coil is directly soldered to the converter board with series capacitors to reduce any contact resistances.

The transmitter and receiver coils are placed one meter far from power converter printed circuit board (PCB) to reduce flux linkage and effects on power transmission. The receiver coil is connected in series with a compensation capacitor followed by a diode bridge rectifier and filter capacitor. This dc power is used to test the loading at various battery voltages and load resistors to check performance at dynamic conditions. The presented results are also following a moderate loading of the battery proposed converter operational performance.

V. RESULTS AND DISCUSSION

The working principle of the proposed converter topology is validated by performing modeling, simulation, and hardware testing. The circuit parameters in simulation and hardware are tuned to an operating point to understand the behavior of the converter.

A. Simulation Results

The simulation of a proposed topology has been done in MATLAB/Simulink by using principal components, as shown in Fig. 4 and Table I. The ideal dc source is placed in series with resistor (nΩ) and inductor (nH). MOSFET switches from SimPowerSystem Library with 0 Ω resistance and 870 pF capacitance as snubber have been used to simulate H-bridge part of dc–dc converter. The auxiliary transformer is contracted by linear transformer and transmitter, receiver coils from mutual inductance.

Fig. 10 shows the ZVS turn-ON of switches S_1 to S_4, as the voltage across the switch reaches to zero, the gate pulse is given to that particular switch to turn it ON. In Fig. 11(a) and (b), the ZCS turn-ON for switches S_2 and S_4 is indicated. The current from the switch becomes zero before the gate pulse finishes. Therefore it is said that the proposed wireless converter maintains ZCZVS. The compensation capacitor voltage peak value is selected by observing the performance of V_{C_1}, as shown in Fig. 12. In Fig. 13, the input side characteristic of the primary network has been shown. These results show the small value of input dc-link capacitors does not affect the performance of the converter.

The performance of the converter for BC is shown in Fig. 14(a)–(d). It is seen from Fig. 14(a) and (b) that the disturbance is very less, whereas the conventional charger having disturbance in BC voltage and current, which reduces the life of the battery and degrades the charger efficiency, whereas the nature of battery voltage and current shown in Fig. 14(c) and (d) is without using the auxiliary circuit. The circuit performance provides 93.5% efficiency with parameters shown in Table I. The output efficiency for fixed parameters is controlled by updating the switching frequency and output power is controlled by changing input voltage. A lookup table has been used to find control parameters. The efficiency characteristics for different loading conditions are shown in Fig. 15. The simulation parameters are

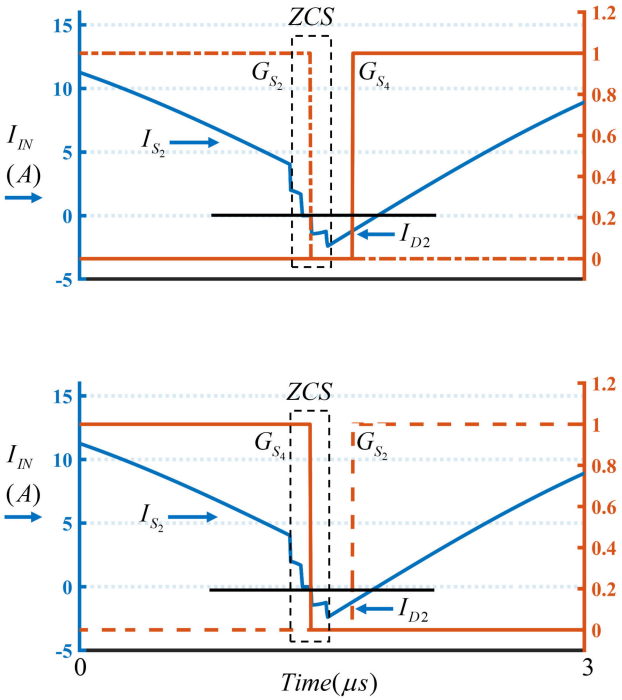

Fig. 11. ZCS turn-OFF for (a) S_2 and (b) S_4.

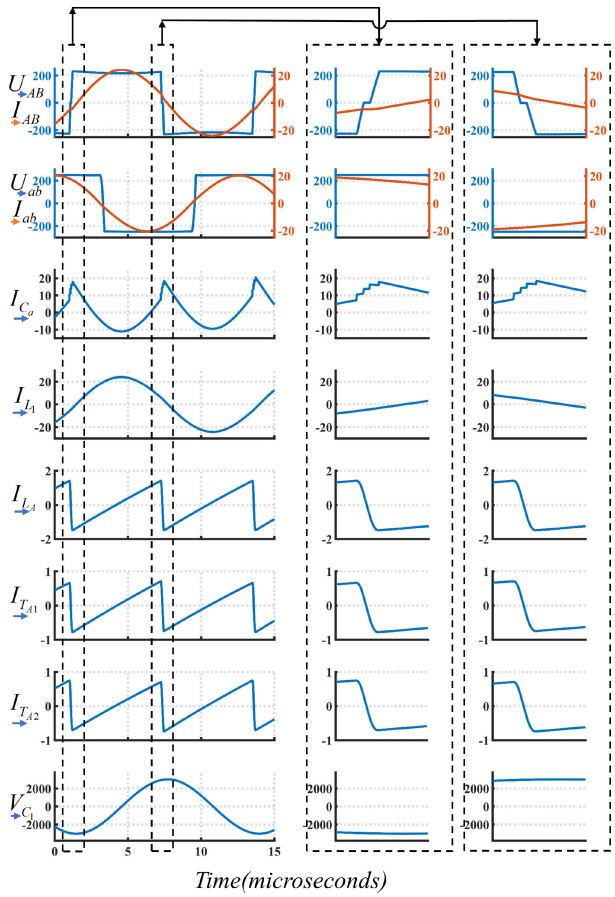

Fig. 12. Converter characteristics waveform in various operating modes.

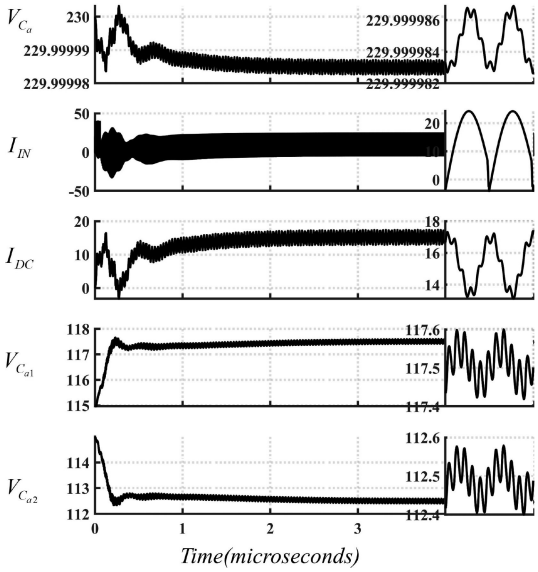

Fig. 13. Input side characteristic of primary network.

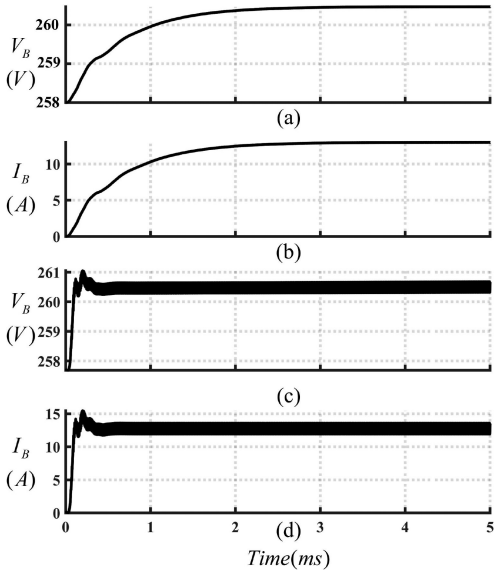

Fig. 14. Output characteristic for BC application.

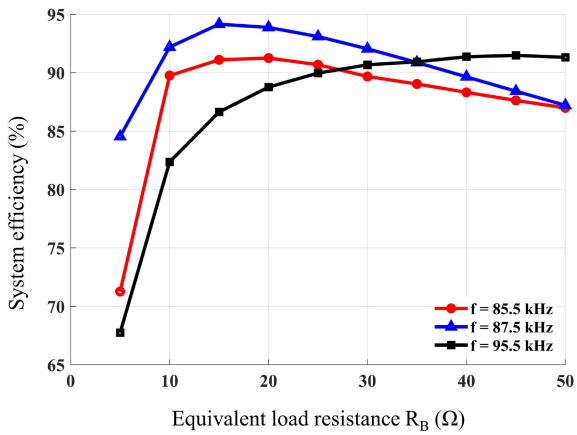

Fig. 15. Frequency response characteristics for different loading conditions.

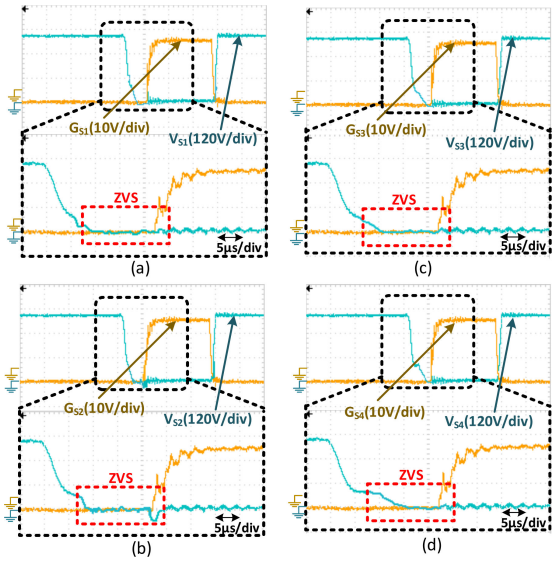

Fig. 16. Experimental results of ZVS turn-ON for (a)–(d) $S_1 - S_4$.

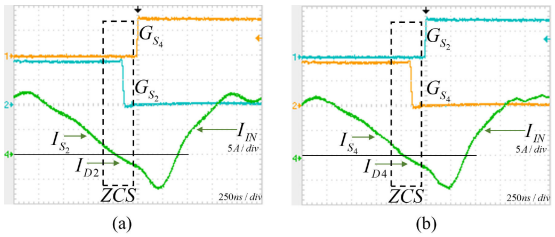

Fig. 17. Experimental results of ZCS turn-OFF for (a) S_2 and (b) S_4.

obtained from component data-sheet and careful study of the developed prototype in the laboratory.

B. Hardware Results

The experimental results of the proposed converter are shown in Figs. 16–20. The developed laboratory prototype is tested for both high-power and low-power BC. The obtained results show the ZCZVS soft switching is obtained for a wide operating range. In Fig. 16(a)–(d), the ZVS turn-ON of switches $S_1 - S_4$ is shown, when the voltage across the switch is zero then the switch will triggered. The ZCS turn-OFF of two low-side switches S_2 and S_4 is shown in Fig. 17(a) and (b).

The voltage appear across primary and secondary of the converter at points A, B and a, b is shown in Fig. 18(a). Fig. 18(b) and (c) shows the voltage across battery and current flowing through L_1. The input current, dc current, and current across capacitor potential divider are shown in Fig. 19(a)–(d), respectively. These results satisfy the theoretical operation as well as simulation of the proposed converter.

Fig. 20(a) shows the BC characteristics for 120-V Li-ion battery with a proposed auxiliary circuit. The current in the circuit is 4.35 A, which delivers 522 W at 91.26% efficiency. Fig. 20(b) shows the BC current and voltage in heavy loading conditions. The delivered power is measured at 1028 W at 91.02% efficiency.

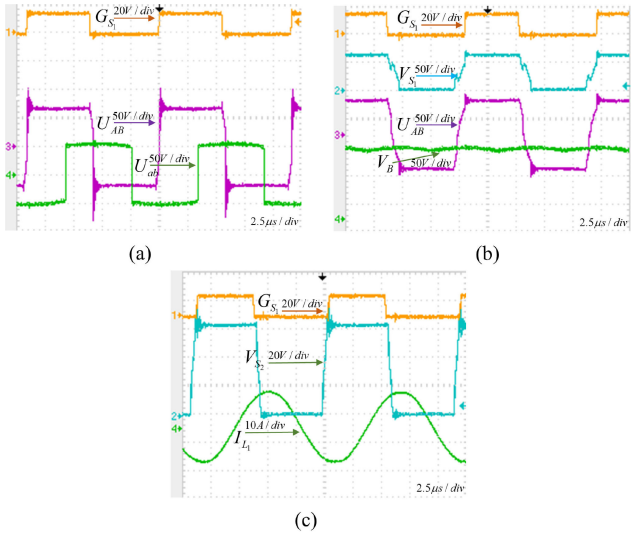

Fig. 18. Laboratory prototype results for (a) voltage across points A, B and a, b, (b) battery voltage w.r.t. voltage across points A and B, and (c) current passing through transmitter coil.

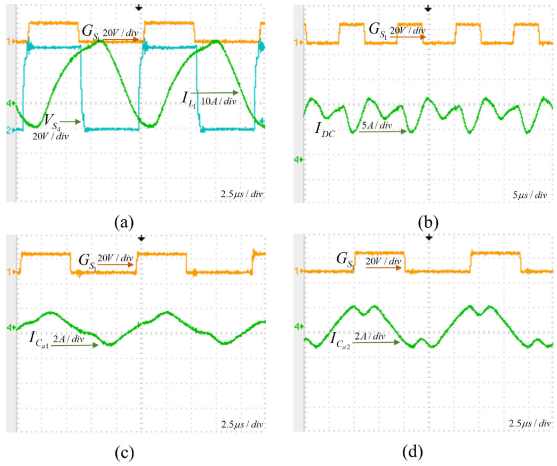

Fig. 19. (a) Input current passing through S_1. (b) DC current coming from supply. (c), (d) Current passing through capacitor potential divider.

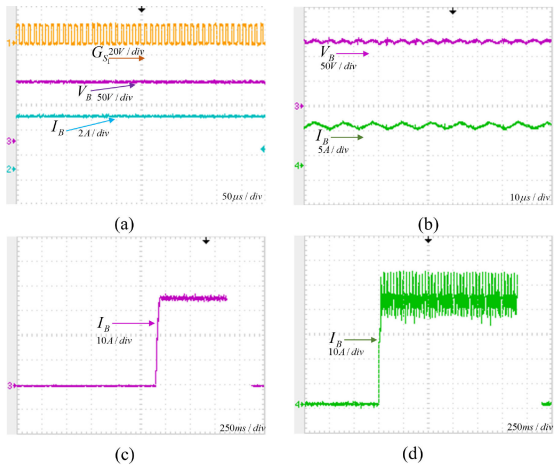

Fig. 20. (a) Battery voltage and current, (b) magnified voltage and current of battery load, transient state of battery current (c) with the proposed auxiliary circuit, and (d) without auxiliary circuit.

The start-up BC characteristics for the proposed auxiliary or the transient current of BC are shown in Fig. 20(c) and without auxiliary network the transient current is shown in Fig. 20(d). It is observed the startup time is less for the proposed circuit but the ripple is high. On the other hand, the spikes are more when no auxiliary circuit has been incorporated.

VI. Conclusion

In this article, the voltage fed series compensation based ZVZCS topology and its tuning method for wireless electrical vehicle battery charger have been proposed. Suitable modifications were presented for the full-bridge dc–dc converter, and enhanced performance with a wide range of input variation is achieved. The need for a high-power processor is eliminated, which further reduces the overall cost. The theoretical analysis and modeling have been presented to obtain ZVZCS with reduced control complexity. The simulation results verified the ZVZCS condition of the proposed topology for a full load range. The offered solution produced less ripple in input/ output voltage and current while utilizing a low value of dc link, and filter capacitance values, respectively. An acceptable efficiency of 91.26% has been achieved for both battery and resistive loads.

References

[1] M. Granovskii, I. Dincer, and M. A. Rosen, "Economic and environmental comparison of conventional, hybrid, electric and hydrogen fuel cell vehicles," *J. Power Sources*, vol. 159, no. 2, pp. 1186–1193, 2006.

[2] S. B. Peterson, J. Whitacre, and J. Apt, "The economics of using plug-in hybrid electric vehicle battery packs for grid storage," *J. Power Sources*, vol. 195, no. 8, pp. 2377–2384, 2010.

[3] Y. Zhou, M. Wang, H. Hao, L. Johnson, and H. Wang, "Plug-in electric vehicle market penetration and incentives: A global review," *Mitigation Adaptation Strategies Global Change*, vol. 20, no. 5, pp. 777–795, 2015.

[4] B. Nykvist and M. Nilsson, "Rapidly falling costs of battery packs for electric vehicles," *Nature Climate Change*, vol. 5, no. 4, pp. 329–332, 2015.

[5] W. Zhang and C. C. Mi, "Compensation topologies of high-power wireless power transfer systems," *IEEE Trans. Veh. Technol.*, vol. 65, no. 6, pp. 4768–4778, Jun. 2016.

[6] K. Mude and K. Aditya, "Comprehensive review and analysis of two-element resonant compensation topologies for wireless inductive power transfer systems," *Chin. J. Elect. Eng.*, vol. 5, no. 2, pp. 14–31, 2019.

[7] Y. Jiang, L. Wang, Y. Wang, J. Liu, X. Li, and G. Ning, "Analysis, design, and implementation of accurate ZVS angle control for EV battery charging in wireless high-power transfer," *IEEE Trans. Ind. Electron.*, vol. 66, no. 5, pp. 4075–4085, May 2019.

[8] Y. Jiang, L. Wang, Y. Wang, J. Liu, M. Wu, and G. Ning, "Analysis, design, and implementation of WPT system for EV's battery charging based on optimal operation frequency range," *IEEE Trans. Power Electron.*, vol. 34, no. 7, pp. 6890–6905, Jul. 2019.

[9] D. H. Tran, V. B. Vu, and W. Choi, "Design of a high-efficiency wireless power transfer system with intermediate coils for the on-board chargers of electric vehicles," *IEEE Trans. Power Electron.*, vol. 33, no. 1, pp. 175–187, Jan. 2018.

[10] S. Moon and G.-W. Moon, "Wireless power transfer system with an asymmetric four-coil resonator for electric vehicle battery chargers," *IEEE Trans. Power Electron.*, vol. 31, no. 10, pp. 6844–6854, Oct. 2016.

[11] O. C. Onar, M. Chinthavali, S. L. Campbell, L. E. Seiber, and C. P. White, "Vehicular integration of wireless power transfer systems and hardware interoperability case studies," *IEEE Trans. Ind. Appl.*, vol. 55, no. 5, pp. 5223–5234, Sep./Oct. 2019.

[12] S. Li, W. Li, J. Deng, T. D. Nguyen, and C. C. Mi, "A double-sided LCC compensation network and its tuning method for wireless power transfer," *IEEE Trans. Veh. Technol.*, vol. 64, no. 6, pp. 2261–2273, Jun. 2015.

[13] C. Liu, S. Ge, Y. Guo, H. Li, and G. Cai, "Double-LCL resonant compensation network for electric vehicles wireless power transfer: Experimental study and analysis," *IET Power Electron.*, vol. 9, no. 11, pp. 2262–2270, 2016.

[14] C. Xiao, D. Cheng, and K. Wei, "An LCC-C compensated wireless charging system for implantable cardiac pacemakers: Theory, experiment, and safety evaluation," *IEEE Trans. Power Electron.*, vol. 33, no. 6, pp. 4894–4905, Jun. 2018.

[15] Y. Chen, H. Zhang, S.-J. Park, and D.-H. Kim, "A switching hybrid LCC-S compensation topology for constant current/voltage EV wireless charging," *IEEE Access*, vol. 7, pp. 133924–133935, 2019.

[16] Y. Zhang, Z. Yan, T. Kan, Y. Liu, and C. C. Mi, "Modelling and analysis of the distortion of strongly-coupled wireless power transfer systems with SS and LCC–LCC compensations," *IET Power Electron.*, vol. 12, no. 6, pp. 1321–1328, 2019.

[17] W. Li, H. Zhao, J. Deng, S. Li, and C. C. Mi, "Comparison study on SS and double-sided LCC compensation topologies for EV/PHEV wireless chargers," *IEEE Trans. Veh. Technol.*, vol. 65, no. 6, pp. 4429–4439, Jun. 2016.

[18] G. N. B. Yadav and N. L. Narasamma, "An active soft switched phase-shifted full-bridge dc–dc converter: Analysis, modeling, design, and implementation," *IEEE Trans. Power Electron.*, vol. 29, no. 9, pp. 4538–4550, Sep. 2014.

[19] M. Pahlevaninezhad, P. Das, J. Drobnik, P. K. Jain, and A. Bakhshai, "A novel ZVZCS full-bridge dc/dc converter used for electric vehicles," *IEEE Trans. Power Electron.*, vol. 27, no. 6, pp. 2752–2769, Jun. 2012.

[20] V. R. K. Kanamarlapudi, B. Wang, P. L. So, and Z. Wang, "Analysis, design, and implementation of an APWM ZVZCS full-bridge dc–dc converter for battery charging in electric vehicles," *IEEE Trans. Power Electron.*, vol. 32, no. 8, pp. 6145–6160, Aug. 2017.

[21] J. K. Nama, M. Srivastava, and A. K. Verma, "Modified inductive power transfer topology for electrical vehicle battery charging using auxiliary network to achieve zero-voltage switching for full load variations," *IET Power Electron.*, vol. 12, no. 10, pp. 2513–2522, 2019.

[22] M. Srivastava, P. S. Tomar, and A. K. Verma, "A modified duty cycle frequency control soft switching of full bridge dc-dc converter for electric vehicle battery charging," in *Proc. 8th IEEE India Int. Conf. Power Electron*, 2018, pp. 1–5.

[23] J. K. Nama, P. S. Tomar, M. Srivastava, and A. K. Verma, "An efficient wireless topology for electric vehicle battery charging," in *Proc. 8th IEEE India Int. Conf. Power Electron.*, 2018, pp. 1–6.

[24] Parashar Vidyut Udyog, Litz Wire—pdf catalogue, 2020. [Online]. Available: https://pdf.indiamart.com/impdf/9435952930/MY-10389389/litz-wire.pdf

[25] Magnetics International, Kool Mμ Hf Powder Cores, 2020. [Online]. Available: https://www.mag-inc.com/Media/Magnetics/File-Library/Product%20Literature/Powder%20Core%20Literature/Magnetics-Kool-M%c2%b5-H%c6%92-Bulletin.pdf

[26] Magnetics International, Ferrite Cores—Toroids | Shapes | Pot Cores, 2020. [Online]. Available: https://www.mag-inc.com/getattachment/Products/Ferrite-Cores/Learn-More-about-Ferrite-Cores/Magnetics-Ferrite-Catalog-2017.pdf?lang=en-US

Jitendra Kumar Nama (Student Member, IEEE) received the B.Tech. degree in electrical engineering from the Rajasthan Technical University, Kota, India, in 2013 and the M.Tech. degree in electrical engineering (power electronics and electrical drivers from the Malaviya National Institute of Technology, Jaipur, India, in 2015, where he is currently working toward the Ph.D. degree with the Department of Electrical Engineering.

His research interests include electric vehicle infrastructure, electric vehicle battery chargers configurations, and wireless dc–dc converters for vehicular application.

Arun Kumar Verma (Senior Member, IEEE) received the master's and Ph.D. degrees from the Indian Institute of Technology Delhi, New Delhi, India, in 2010 and 2015, respectively.

He was a Postdoctoral Research Fellow with the Energy Research Institute, Nanyang Technological University (NTU) Singapore, during 2015–2016. Prior to joining NTU Singapore, he was a Visiting Graduate Researcher with the Smart Grid Energy Research Centre, University of California–Los Angeles, Los Angeles, CA, USA, during 2014–2015. He is currently an Assistant Professor with the Department of Electrical Engineering, Malaviya National Institute of Technology, Jaipur, India. His research interests include power electronics, power conversion techniques, solar PV inverter, power quality, smart grid and smart building, electric vehicle (EV), EV chargers, and bidirectional power flow.

Dr. Verma was the recipient of the prestigious POSOCO Power System Research Award in 2016 and also won the prestigious BASE fellowship for advanced solar energy research in 2014.

Manaswi Srivastava (Student Member, IEEE) received the B.Tech. degree in electrical and electronics engineering from the Gautam Buddh Technical University (now, Dr. A. P. J. Abdul Kalam Technical University), Lucknow, India, in 2012 and the M.Tech. degree in electrical engineering (power electronics and electrical drivers) from the GLA University, Mathura, India, in 2016. He is currently working toward the Ph.D. degree with the Department of Electrical Engineering, Malaviya National Institute of Technology, Jaipur, India.

Prior to M.Tech., he was a Graduate Engineer Trainee with KEC International Limited, Nagpur, India, in SBU-Railways. His research interests include electric vehicle infrastructure, electric vehicle battery chargers configurations, and wireless dc–dc converters for vehicular application.

Pavan Singh Tomar (Student Member, IEEE) received the B.Tech. degree in electrical engineering from Government Engineering College, Ajmer, India, in 2012 and the M.Tech. degree in power electronics and electrical drivers from the University College of Engineering, Kota, India, in 2017. He is currently working toward the Ph.D. degree with the Department of Electrical Engineering, Malaviya National Institute of Technology, Jaipur, India.

Prior to M.Tech., he was an Assistant Professor with the Arya Institute of Engineering and Technology, Jaipur, India. His research interests include investigations on novel uni-/bidirectional dc–dc converters for electric vehicular applications.